

ShaSTA: Modeling Shape and Spatio-Temporal Affinities for 3D Multi-Object Tracking

Tara Sadjadpour¹, Jie Li², Rares Ambrus², and Jeannette Bohg¹

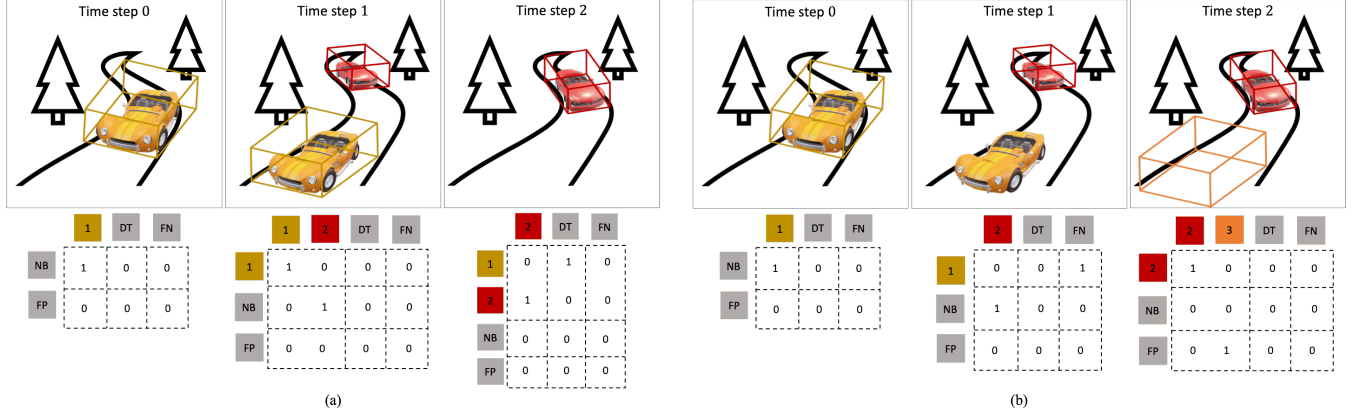


Fig. 1: Examples for tracking scenarios (top) and associated ground-truth affinity matrices (bottom) that our algorithm, ShaSTA, has to estimate. In all affinity matrices, the rows correlate with previous frame tracks that are represented with single-history bounding box detections, while the columns correlate with current frame detections. The affinity matrices are augmented with two rows for *newborn track* (NB) and *false-positive* (FP) anchors that the current frame detections can match with, and two columns for *dead track* (DT) and *false-negative* (FN) anchors that the previous frame tracks can match with. These four augmentations are learned representations that capture the essence of these four detection and track types for each frame. The bounding box color corresponds to the track ID. At time step $t = 0$, both figures (a) and (b) start with affinity matrix A_0 , where the yellow car is detected and is matched with NB, thus initializing Track 1. For Figure (a), at $t = 1$, A_1 shows that the yellow car is detected again and matched with the previous frame's Track 1, while the red car is detected as a newborn with Track ID 2. Then, at $t = 2$, there is only one detection for the red car, so it is matched with the previous frame's Track 2, while Track 1 is matched with DT in A_2 . In Figure (b), at time step $t = 1$, the red car is detected as a newborn with Track ID 2, while the yellow car is not detected at all so Track 1 from $t = 1$ is matched with FN. Finally, at $t = 2$, the red car is detected again and matched with Track 2, while a detection is found in a region with no object so it is matched with FP in A_2 .

Abstract—Multi-object tracking is a cornerstone capability of any robotic system. Most approaches follow a tracking-by-detection paradigm. However, within this framework, detectors function in a low precision-high recall regime, ensuring a low number of false-negatives while producing a high rate of false-positives. This can negatively affect the tracking component by making data association and track lifecycle management more challenging. Additionally, false-negative detections due to difficult scenarios like occlusions can negatively affect tracking performance. Thus, we propose a method that learns shape and spatio-temporal affinities between consecutive frames to better distinguish between true-positive and false-positive detections and tracks, while compensating for false-negative detections. Our method provides a probabilistic matching of detections that leads to robust data association and track lifecycle management. We quantitatively evaluate our method through ablation experiments and on the nuScenes tracking benchmark where we achieve state-of-the-art results. Our method not only estimates accurate, high-quality tracks but also decreases the overall number of false-positive and false-negative tracks. Please see our project website for source code and demo videos: sites.google.com/view/shasta-3d-mot/home.

I. INTRODUCTION

In this work, we address the problem of 3D multi-object tracking using LiDAR point cloud data as input. 3D multi-object tracking is an essential capability of autonomous agents to navigate effectively in their environments. For example, autonomous cars need to understand where all the traffic actors in their surroundings are such that they can safely drive. Online tracking is achieved by accurately

matching uncertain detections to existing tracks and determining when to initialize and terminate tracks. These two processes are often referred to as *data association* and *track lifecycle management*. Most recent approaches toward 3D multi-object tracking in autonomous driving apply the tracking-by-detection paradigm. Though this framework has been successful, a practical gap between state-of-the-art 3D detection and tracking lies in the evaluation protocols. Since 3D detectors are mainly evaluated on the full recall spectrum of detections (e.g., mAP [1]), they tend to generate high rates of false-positives to ensure a low number of false-negatives [2, 3]. These redundant detections lead to highly cluttered outputs that make data association and track lifecycle management more challenging. Additionally, occasional false-negative detections due to factors such as heavy occlusion can cause significant fragmentations in the tracks or lead to the premature termination of tracks. Recent works in LiDAR-only and multi-modal tracking-by-detection [4–7] have attempted to develop learning-based and statistical approaches to better handle data association, false-positive elimination, false-negatives propagation, and track lifecycle management. However, these approaches do not leverage spatio-temporal and shape information from the LiDAR sensor input, and in some cases, only rely on detected bounding box parameters as their input information.

Our **main contribution** is a 3D multi-object tracking technique called *ShaSTA* that models **shape** and **spatio-temporal** affinities between tracks and detections in consecutive frames to jointly conduct data association, false-positive (FP) elimination, false-negative (FN) propagation, newborn (NB) initialization, and dead track (DT) termination. The core

¹ Stanford University, {tsadja, bohg}@stanford.edu

² Toyota Research Institute, {jie.li, rares.ambrus}@tri.global

novelty of our approach is that we leverage spatio-temporal and shape information to model the similarity between detections and tracks. *ShaSTA* also learns representations of FP, NB, FN, and DT *anchors* for each frame. By computing the affinity between detections and tracks to these learned representations, we can classify detections as newborn tracks or false-positives, while tracks can be classified as dead tracks or false-negatives. This approach not only aids in tracking performance but also addresses concerns for real-world deployment and downstream decision-making tasks by eliminating false-positive tracks and minimizing track fragmentations. *ShaSTA* offers an efficient and practical implementation that can re-use the LiDAR backbone of most off-the-shelf LiDAR-based 3D detectors. Without loss of generality, we choose the LiDAR backbone from CenterPoint [2] for a fair comparison against most previous works. We demonstrate that our approach achieves state-of-the-art results on the nuScenes tracking benchmark where we achieve significant gains in overall tracking accuracy and precision. We also include ablation studies to analyze the contribution of each component.

II. RELATED WORK

A. LiDAR-based 3D Detection

Most recent 3D multi-object tracking (3D MOT) works follow the tracking-by-detection paradigm [4–9], making 3D detectors a key component in tracking systems. LiDAR-based 3D detectors extend the image-based 2D detection algorithms [10, 11] to 3D. The typical detector starts with an encoder [12–14] applied to unstructured point cloud data to extract an intermediate 3D feature grid [3] or bird’s-eye-view (BEV) feature map [2, 15]. Then, a decoder is applied to extract objectness [16] and detailed object attributes [2, 17]. Our approach proposes leveraging the intermediate BEV feature map for robust multi-object tracking, which can be generalized to most modern 3D detectors. In this work, we apply CenterPoint [2] for fair comparison against other trackers.

B. 3D Multi-Object Tracking

With the advances in 3D detection, the 3D MOT community has been focusing on three directions to establish robust tracking within the tracking-by-detection paradigm: motion prediction, data association, and track lifecycle management.

In 3D MOT, abstracted detection predictions are often used for motion prediction and data association, which is completed using pair-wise feature distance between tracks and detections [2, 8, 18]. AB3DMOT [8] provides a baseline to combine Kalman Filters and Intersection Over Union (IOU) association for 3D multi-object tracking. Followup works in this line explore variations of data association metrics, such as the Mahalanobis distance to leverage uncertainty measurements in the Kalman Filter [18]. As an alternative, CenterPoint [2] uses high-fidelity instance velocity predictions as a motion model to complete data association. Unlike these works that only use low-dimensional bounding boxes and explicit motion models for tracking, we propose to leverage intermediate representations

from a detection network for richer information about each object, while also modeling the global relationship of all the objects in a scene to improve data association.

Additionally, track lifecycle management has been reasonably successful with heuristics that are tuned to each dataset [2, 8, 18], but these hand-tuned techniques have shortcomings in more complex situations. Recently, OGR3MOT [4] has proposed combining tracking and predictive modeling through a unified graph representation that learns data associations and track lifecycle management, FP elimination, and FN interpolation. Additionally, [5] proposes a statistical approach for data association under a Bayesian estimation framework. Though these techniques yield competitive results compared to heuristics, their main shortfall is their inability to capture object shape information. Unlike these techniques, our approach leverages raw LiDAR data to capture spatio-temporal and shape information about objects in our scene, which we can use to further improve tracking performance.

Another line of 3D MOT algorithms focuses on using multi-modal data [6, 7, 19, 20]. Similar to our approach, MultimodalTracking [6] learns FP suppression and NB initialization while using intermediate BEV features. Likewise, DeepFusionMOT [7] learns track lifecycle management using deep association, where distant objects are tracked with a camera, and their trajectories are updated with 3D information once they are in the LiDAR field-of-view. Nonetheless, these two methods address these issues from a camera-LiDAR sensor fusion standpoint, while our approach does not rely on multi-modal information to achieve competitive results due to our effective use of spatio-temporal and shape information from the LiDAR sensor.

III. SHASTA

Our algorithm operates under the tracking-by-detection paradigm and is visualized in Fig. 2. *ShaSTA* extracts spatio-temporal and shape relationships between consecutive frames to learn affinity matrices that capture associations between detections and tracks. *ShaSTA* learns bounding box and shape representations for FP, NB, FN, and DT *anchors*, where each anchor captures the common features between the set of detections and tracks that falls under each of these four categories in a given frame. Thus, *ShaSTA*’s affinity matrices not only estimate the probabilities of previous frame tracks matching with current frame detections, but also considers previous frame tracks matching with DT or FN anchors and current frame detections matching with NB or FP anchors. Unlike past techniques that only use low-dimensional bounding box representations, *ShaSTA* leverages spatio-temporal and shape information from the LiDAR sensor input, resulting in a robust data association technique that effectively accounts for FP elimination, FN propagation, NB initialization, and DT termination.

A. Affinity Matrix Usage for Online Tracking

Allowing for up to N_{max} detections per frame, *ShaSTA* estimates two affinity matrices: $A_1 \in \mathbb{R}^{N_{max} \times (N_{max}+2)}$ for

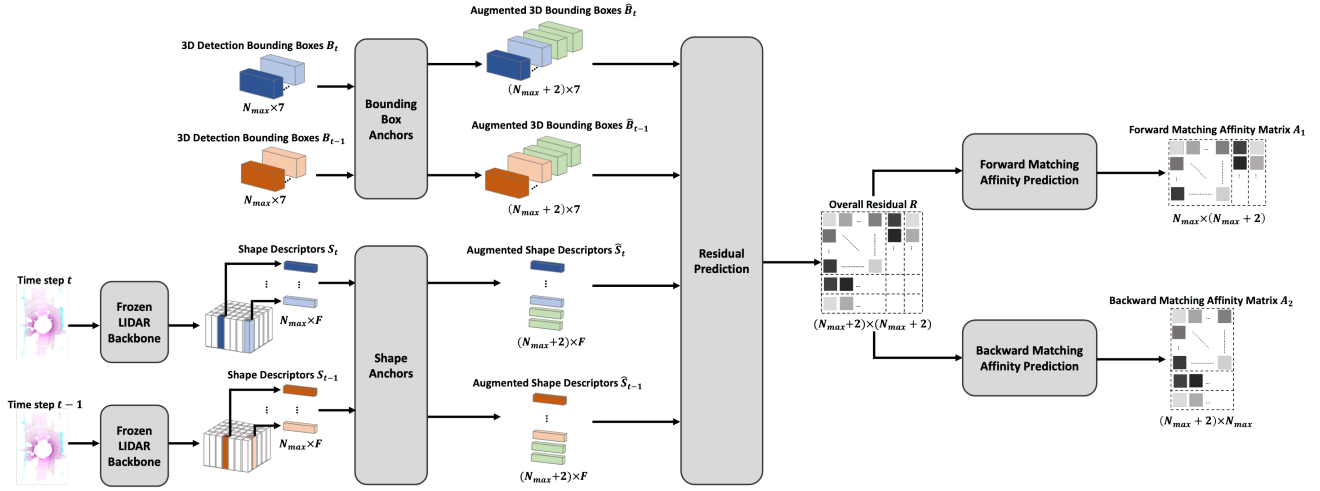


Fig. 2: Algorithm Flowchart. Going from top to bottom and left to right, ShaSTA uses N_{max} low-dimensional bounding boxes from the current and previous frames to learn bounding box representations for the FP, NB, FN, and DT anchors. The FP and NB anchors are appended to previous frame bounding boxes to form the augmented bounding boxes \hat{B}_{t-1} , while the FN and DT anchors are added to the current frame detections to form the augmented bounding boxes \hat{B}_t . Using the pre-trained frozen LiDAR backbone from our off-the-shelf detector, we extract shape descriptors that are then used to learn shape representations for our anchors. The learned shape representations for the anchors are appended to create augmented shape descriptors. These augmented bounding boxes and shape descriptors are then used to find a residual that captures the spatio-temporal and shape similarities between current and previous frame detections, as well as between detections and anchors. The residual is then used to predict forward matching and backward matching affinity matrices for probabilistic data associations, track lifecycle management, FP elimination, and FN propagation.

forward matching and $A_2 \in \mathbb{R}^{(N_{max}+2) \times N_{max}}$ for backward matching. Forward matching indicates that we want to find the best current frame match for each previous frame track, while backward matching refers to finding the best previous frame match for each current frame detection. Since previous frame tracks can match with DT or FN, the forward matching affinity matrix A_1 has two augmented columns for the DT and FN anchors. Similarly, because current frame detections can match with NB or FP, the backward matching affinity matrix A_2 has two augmented rows for the NB and FP anchors.

To form tracks, we combine the affinity matrix outputs and the matching algorithm from [2] as follows. We take A_1 and label any previous frame track that has a probability above the threshold τ_{dt} in the DT column as a DT, and we forward propagate any previous frame track into the current frame if it has a probability above the threshold τ_{fn} in the FN column. In addition to provided detections, *forward propagation* creates a new detection for the current frame to handle occluded objects that off-the-shelf detections missed. We create a box in the current frame $b'_t := (x', y', z, w, l, h, r_y)$, by moving the 2D center coordinate of the existing track $b_{t-1} := (x, y, z, w, l, h, r_y)$ to the next frame based on the estimated velocity provided by our off-the-shelf 3D detector and Δt between the two frames, i.e. $x' = x + v_x \Delta t$ and $y' = y + v_y \Delta t$. All previous frame tracks that do not qualify as FN or DT are kept as is. Analogously, we take A_2 and remove any current frame detection that has a probability above the threshold τ_{fp} in the FP row and we label any current frame detection that has a value above the threshold τ_{nb} in the NB row as an NB. All current frame detections that do not qualify as FP or NB are kept as is. See section V for details on the threshold values we choose.

With these detections, we then run the greedy algorithm from [2]. In its original form, the greedy algorithm takes all unmatched detections and initializes NBs with them. We

instead check if an unmatched detection is labeled as an NB in the affinity matrix based on the threshold τ_{nb} and whether it is outside the maximum distance threshold with respect to other tracks to initialize it as an NB. Otherwise, it is discarded. Additionally, we check if an unmatched track is labeled as a DT based on the threshold τ_{dt} and whether it is outside the maximum distance threshold with respect to other detections to terminate it as a DT.

B. Learning to Predict Affinity Matrices

ShaSTA uses off-the-shelf 3D detections, as well as the pre-trained LiDAR backbone used to generate the detections. ShaSTA first learns bounding box and shape representations for the anchors so we can later use this information to learn a residual that encodes spatio-temporal and shape similarities not only between current frame detections and previous frame tracks, but also between current frame detections and FP and NB anchors or between previous frame tracks and FN and DT anchors. The residual is then used to predict affinity matrices that assign probabilities for matching detections to tracks, eliminating FPs, propagating FNs, initializing NBs, and terminating DTs.

1) *Learning Bounding Box Representations for Anchors:* Our goal is to learn bounding box representations for each of the FP, FN, NB, and DT anchors in a given frame pair. The aim of the bounding box representation of each anchor is to capture the commonalities between detection bounding boxes that fall under each of these four categories.

We use off-the-shelf 3D detections, which provide us with 3D bounding box representations that include each box's center coordinate, dimensions, and yaw rotation angle: $b := (x, y, z, w, l, h, r_y)$. We take the set of bounding boxes for the current frame $B_t \in \mathbb{R}^{N_{max} \times 7}$ and previous frame $B_{t-1} \in \mathbb{R}^{N_{max} \times 7}$. We fix the maximum number of bounding boxes we take per frame to be N_{max} ; we zero pad the matrix if there are fewer than N_{max} bounding boxes,

and we sample the top N_{max} detection bounding boxes if there are greater than N_{max} boxes.

Then, we create a learned bounding box representation for FP and NB anchors using the current frame detections B_t as follows, where each σ represents an MLP:

$$d_{fp} = \sigma_{fp}^d(B_t) \quad (1)$$

$$d_{nb} = \sigma_{nb}^d(B_t). \quad (2)$$

Similarly, we find learned bounding box representations for FN and DT anchors using previous frame detections B_{t-1} :

$$d_{fn} = \sigma_{fn}^d(B_{t-1}) \quad (3)$$

$$d_{dt} = \sigma_{dt}^d(B_{t-1}). \quad (4)$$

For all four cases, we apply the absolute value to the MLP outputs corresponding to (w, l, h) , since dimensions need to be non-negative values. We then concatenate $b_{fp} \in \mathbb{R}^7$ and $b_{nb} \in \mathbb{R}^7$ to B_{t-1} to get $\hat{B}_{t-1} \in \mathbb{R}^{(N_{max}+2) \times 7}$, as well as $b_{fn} \in \mathbb{R}^7$ and $b_{dt} \in \mathbb{R}^7$ to B_t to get $\hat{B}_t \in \mathbb{R}^{(N_{max}+2) \times 7}$. The reason we append FP and NB anchors to B_{t-1} is so that current frame detections can match to them, and the same logic applies for appending FN and DT anchors to B_t .

2) Learning Shape Representations for Anchors: In this section, we extract shape descriptors for each 3D detection using the pre-trained LiDAR backbone of our off-the-shelf detector to leverage spatio-temporal and shape information from the raw LiDAR data. In similar fashion to the previous section, our goal is to learn shape representations for the FP, FN, NB, and DT anchors using the shape descriptors from existing detections. These shape descriptors will be used to match detections to each other or one of the anchors if they share similar shape information.

We pass the current frame's 4D LiDAR point cloud with an added temporal dimension into the frozen pre-trained VoxelNet [3] LiDAR backbone used in the CenterPoint [2] detector. This outputs a bird's-eye-view (BEV) map for the current frame, where each voxelized region encodes a high-dimensional volumetric representation of the shape information in that region. Then, for each current frame detection bounding box, we extract a shape descriptor using bilinear interpolation from the BEV map as in [2] using the bounding box center, left face center, right face center, front face center, and back face center. We concatenate these 5 shape features to create the overall shape feature for each bounding box. Note that in BEV, the box center, bottom face center, and top face center all project to the same point, so we forgo extracting the latter two centers. We accumulate all of the shape features extracted for the current frame detections and call this cumulative shape descriptor, $S_t \in \mathbb{R}^{N_{max} \times F}$. We repeat the same procedure for the previous frame's LiDAR point cloud and bounding boxes to get the overall shape descriptor $S_{t-1} \in \mathbb{R}^{N_{max} \times F}$.

Using the extracted shape features for the current frame S_t , we obtain our learned shape descriptors for the FP and

NB anchors with MLPs σ_{fp} and σ_{nb} , respectively:

$$s_{fp} = \sigma_{fp}^s(S_t) \quad (5)$$

$$s_{nb} = \sigma_{nb}^s(S_t). \quad (6)$$

Likewise, we use our previous frame's shape features S_{t-1} to learn shape descriptors for FN and DT anchors as such:

$$s_{fn} = \sigma_{fn}^s(S_{t-1}) \quad (7)$$

$$s_{dt} = \sigma_{dt}^s(S_{t-1}). \quad (8)$$

Just as we did in the previous section, we concatenate $s_{fp} \in \mathbb{R}^F$ and $s_{nb} \in \mathbb{R}^F$ to S_{t-1} to get the augmented shape descriptor $\hat{S}_{t-1} \in \mathbb{R}^{(N_{max}+2) \times F}$, as well as $s_{fn} \in \mathbb{R}^F$ and $s_{dt} \in \mathbb{R}^F$ to S_t to get $\hat{S}_t \in \mathbb{R}^{(N_{max}+2) \times F}$.

3) Residual Prediction: Using the augmented 3D bounding boxes and shape descriptors, we aim to find three residuals that measure the similarities between current and previous frames' bounding box and shape representations. Since the boxes are low-dimensional abstractions, we obtain two residuals for the augmented 3D bounding boxes called the VoxelNet and bounding box residuals, R_v and R_b respectively. We also learn one shape residual R_s between the augmented shape descriptors. We obtain our overall residual R that captures the spatio-temporal and shape similarities by taking a weighted sum of the three residuals, where the weights are also learned.

VoxelNet Residual. Our first residual $R_v \in \mathbb{R}^{(N_{max}+2) \times (N_{max}+2)}$ is a variation of the VoxelNet [3] bounding box residual. We adapt the VoxelNet residual for the end-goal of data association between \hat{B}_{t-1} and \hat{B}_t to capture their similarities based on box center, dimension, and rotation.

Bounding Box Residual. The learned bounding box residual $R_b \in \mathbb{R}^{(N_{max}+2) \times (N_{max}+2)}$ is found by first expanding \hat{B}_{t-1} and \hat{B}_t and concatenating them to get a matrix $\hat{B} \in \mathbb{R}^{(N_{max}+2) \times (N_{max}+2) \times 6}$. Note that for this step we only use the box centers from \hat{B}_{t-1} and \hat{B}_t . Then, we obtain our residual $R_b \in \mathbb{R}^{(N_{max}+2) \times (N_{max}+2)}$ with an MLP σ_r^b as such:

$$R_d = \sigma_r^d(\hat{B}). \quad (9)$$

Shape Residual. We use \hat{S}_t and \hat{S}_{t-1} to obtain the learned shape residual R_s between the two frames. We expand \hat{S}_{t-1} and \hat{S}_t and concatenate them to get a matrix $\hat{S} \in \mathbb{R}^{(N_{max}+2) \times (N_{max}+2) \times 2F}$. Then, we obtain our residual $R_s \in \mathbb{R}^{(N_{max}+2) \times (N_{max}+2)}$ with an MLP:

$$R_s = \sigma_r^s(\hat{S}). \quad (10)$$

Overall Residual. The overall residual R is a weighted sum of the three residuals we previously obtained: R_v , R_b , and R_s . We concatenate \hat{B} and \hat{S} that we previously obtained in the early steps to create our input $\hat{W} \in \mathbb{R}^{(N_{max}+2) \times (N_{max}+2) \times (2F+6)}$. Then, we pass this through an MLP σ_α to get the learned weights $\alpha \in \mathbb{R}^{(N_{max}+2) \times (N_{max}+2) \times 3}$ as follows:

$$\alpha = \sigma_\alpha(\hat{W}). \quad (11)$$

We split α into matrices $\alpha_v, \alpha_b, \alpha_s \in \mathbb{R}^{(N_{max}+2) \times (N_{max}+2)}$, and obtain our overall residual $R \in \mathbb{R}^{(N_{max}+2) \times (N_{max}+2)}$:

$$R = \alpha_v \odot R_v + \alpha_b \odot R_b + \alpha_s \odot R_s. \quad (12)$$

Note that \odot is the Hadamard product.

4) *Affinity Matrix Estimation*: Given our overall residual, we have information about the pairwise similarities between current frame detections and previous frame tracks, as well as each of the four augmented anchors. We want to use these spatio-temporal and shape relationships to learn probabilities for matching the detections and tracks to each other or the anchors. This will ultimately allow us to leverage global relationships for learning our matching probabilities, as opposed to using greedy local searches on residuals for matching [2, 18]. We find a forward matching affinity matrix and a backward matching affinity matrix to learn data association in both directions, while ensuring that we do not mix matching of DT and FN anchors with NB and FP anchors.

Forward Matching Affinity Matrix. We remove the augmented rows corresponding to NB and FP from the overall residual R to obtain $R_1 \in \mathbb{R}^{N_{max} \times (N_{max}+2)}$. We then apply an MLP and row-wise softmax (each row adds to probability of 1) to get our forward matching affinity matrix $A_1 \in \mathbb{R}^{N_{max} \times (N_{max}+2)}$:

$$A_1 = \text{softmax}_{\text{row}}(\sigma_{fm}(R_1)). \quad (13)$$

Backward Matching Affinity Matrix. In order to obtain our backward matching affinity matrix $A_2 \in \mathbb{R}^{(N_{max}+2) \times N_{max}}$, we remove the augmented columns corresponding to DT and FN from the overall residual R to obtain $R_2 \in \mathbb{R}^{(N_{max}+2) \times N_{max}}$ and we apply an MLP and column-wise softmax:

$$A_2 = \text{softmax}_{\text{col}}(\sigma_{bm}(R_2)). \quad (14)$$

C. Log Affinity Loss

Inspired by [21–23], we define the log affinity loss \mathcal{L}_{la} , based on the ground-truth affinity matrix A_{gt} and the estimated affinity matrix A as follows with Hadamard product \odot :

$$\mathcal{L}_{la} = \frac{\sum_i \sum_j (A_{gt} \odot -\log(A))}{\sum_i \sum_j A_{gt}}. \quad (15)$$

For our model, we have two outputs $A_1 \in \mathbb{R}^{N_{max} \times (N_{max}+2)}$ and $A_2 \in \mathbb{R}^{(N_{max}+2) \times N_{max}}$ with corresponding ground-truth affinity matrices $A_{gt,1}$ and $A_{gt,2}$. Furthermore, we have $\hat{A}_1, \hat{A}_2 \in \mathbb{R}^{N_{max} \times N_{max}}$, where we remove the augmented columns for DT and FN and augmented rows for NB and FP respectively. The corresponding ground-truth for these two matrices is $A_{gt,3}$.

Thus, our overall loss function \mathcal{L} is defined as follows:

$$\mathcal{L}_{fm} = \frac{\sum_i \sum_j (A_{gt,1} \odot -\log(A_1))}{\sum_i \sum_j A_{gt,1}} \quad (16)$$

$$\mathcal{L}_{bm} = \frac{\sum_i \sum_j (A_{gt,2} \odot -\log(A_2))}{\sum_i \sum_j A_{gt,2}} \quad (17)$$

$$\mathcal{L}_m = \frac{\sum_i \sum_j (A_{gt,3} \odot -\log(\max(\hat{A}_1, \hat{A}_2)))}{\sum_i \sum_j A_{gt,3}} \quad (18)$$

$$\mathcal{L}_a = \|\hat{A}_1 - \hat{A}_2\|_1 \quad (19)$$

$$\mathcal{L} = \frac{1}{4}(\mathcal{L}_{fm} + \mathcal{L}_{bm} + \mathcal{L}_m + \mathcal{L}_a) \quad (20)$$

IV. DATA PREPARATION

We evaluate our tracking performance on the nuScenes benchmark [24]. The nuScenes dataset contains 1000 scenes, where each scene is 20 seconds long and is generated with a 2Hz frame-rate. For the tracking task, nuScenes has 7 classes: bicycle, bus, car, motorcycle, pedestrian, trailer, and truck. In this section, we provide an overview of the LiDAR preprocessing and ground-truth affinity matrix formation we complete to deploy ShaSTA for the nuScenes dataset.

A. LiDAR Point Cloud Preprocessing

Since CenterPoint [2] provides detections at 2Hz, but the LiDAR has a sampling rate of 20Hz, we use the nuScenes [24] feature for accumulating multiple LiDAR sweeps with motion compensation. This provides us with a denser 4D point cloud with an added temporal dimension, and makes the LiDAR input match the detection sampling rate. We use 10 LiDAR sweeps to generate the point cloud.

B. Ground-Truth Affinity Matrix.

We find the true-positive, false-positive, and false-negative detections using the matching algorithm from the nuScenes [24] dev-kit. For each frame, we define a ground-truth affinity matrix $A_t \in \mathbb{R}^{(N_{max}+2) \times (N_{max}+2)}$ between the current frame and previous frame off-the-shelf detections. For all true-positive previous and current frame detections, B_{t-1}^{tp} and B_t^{tp} , we say they are matched if the ground-truth boxes they each correspond to have the same ground-truth tracking IDs. If there is a match between true-positive boxes $b_{t-1,i}^{tp} \in B_{t-1}^{tp}$ and $b_{t,j}^{tp} \in B_t^{tp}$, then $A_t(i, j) = 1$. For all false-positive previous frame detections and true-positive previous frame detections whose tracking IDs do not appear in any of the current frame ground-truth tracking IDs, we call them dead tracks B_{t-1}^{dt} . For all $b_{t-1,i}^{dt} \in B_{t-1}^{dt}$, we set $A_t(i, N_{max} + 1) = 1$. For all true-positive previous frame detections that do not have a match in the current frame but whose tracking IDs do appear in the current frame ground-truth tracking IDs, we call them false-negatives B_{t-1}^{fn} . For all $b_{t-1,i}^{fn} \in B_{t-1}^{fn}$, we set $A_t(i, N_{max} + 2) = 1$. Additionally, for all true-positive current frame detections whose tracking IDs do not appear in the previous frame ground-truth tracking IDs, we call them newborn tracks B_t^{nb} , and we set $A_t(N_{max} + 1, j) = 1$ for all $b_{t,j}^{nb} \in B_t^{nb}$. Finally, we define the set of false-positive current frame

TABLE I: nuScenes Test Results with evaluation in terms of overall and individual AMOTA and AMOTP. We only compare on methods that use CenterPoint detections. White entries are LiDAR-only, while gray entries are camera-LiDAR fusion. The blue entry is our LiDAR-only method ShaSTA.

Metric	Method	Input	Overall	Bicycle	Bus	Car	Motorcycle	Pedestrian	Trailer	Truck
AMOTA \uparrow	CenterPoint [2]	3D	65.0	33.1	71.5	81.8	58.7	78.0	69.3	62.5
	OGR3MOT [4]	3D	65.6	38.0	71.1	81.6	64.0	78.7	67.1	59.0
	ShaSTA (Ours)	3D	67.3	32.4	73.2	84.0	67.1	80.1	69.3	64.7
	MultimodalTracking [6]	2D+3D	65.5	46.9	71.3	83.0	63.1	74.1	65.7	54.6
	DeepFusionMOT [7]	2D+3D	63.5	52.0	70.8	72.5	69.6	55.4	64.9	59.6
AMOTP \downarrow	CenterPoint [2]	3D	0.535	0.561	0.636	0.391	0.519	0.409	0.729	0.5
	OGR3MOT [4]	3D	0.620	0.899	0.675	0.395	0.615	0.383	0.790	0.585
	ShaSTA (Ours)	3D	0.536	0.675	0.630	0.382	0.498	0.370	0.709	0.484
	MultimodalTracking [6]	2D+3D	0.617	0.895	0.677	0.388	0.561	0.507	0.753	0.540
	DeepFusionMOT [7]	2D+3D	0.668	0.934	0.630	0.540	0.704	0.559	0.744	0.563

TABLE II: nuScenes Test Results with evaluation in terms of overall TP, FP, and FN. White entries are LiDAR-only, while gray entries are camera-LiDAR fusion. The blue entry is our LiDAR-only method ShaSTA.

Method	Input	TP \uparrow	FP \downarrow	FN \downarrow
CenterPoint [2]	3D	94,324	17,355	24,557
OGR3MOT [4]	3D	95,264	17,877	24,013
ShaSTA (Ours)	3D	96,469	15,821	22,519
MultimodalTracking [6]	2D+3D	95,199	18,061	23,323
DeepFusionMOT [7]	2D+3D	84,304	19,303	33,556

detections as B_t^{fp} , and we set $A_t(N_{max} + 2, j) = 1$ for all $b_{t,j}^{fp} \in B_t^{fp}$. Unmatched (i, j) entries are set to 0.

V. EXPERIMENTAL RESULTS

This section provides an overview of evaluation metrics, training details, comparisons against state-of-the-art 3D multi-object tracking techniques, and ablation studies to analyze our technique.

A. Evaluation Metrics

The primary metrics for evaluating nuScenes are Average Multi-Object Tracking Accuracy (AMOTA) and Average Multi-Object Tracking Precision (AMOTP) [25]. AMOTA measures the ability of a tracker to track objects correctly, while AMOTP measures the quality of the estimated tracks. We direct readers to [25] for a more thorough definition of the metrics. We also present secondary metrics, including the total number of true-positives (TP), FPs, and FNs to better analyze the effectiveness of our approach.

B. Training Specifications

We train a different network for each object category following [6, 26]. The value of N_{max} depends on the object type since some classes are more common than others. We choose the value for N_{max} based on the per-object detection frequency we gather in the training set. The smallest is $N_{max} = 20$ and the largest is $N_{max} = 90$. We use the Adam optimizer with a constant learning rate of 10^{-4} and L2 weight regularization of 10^{-2} . We use the pre-trained VoxelNet weights from CenterPoint [2] and freeze them for our LiDAR backbone so that the shape information correlates with our detection bounding boxes from [2]. Additionally, there is a significant class imbalance between FPs and TPs since state-of-the-art detectors function in low precision-high recall regimes. Thus, we downsample the number of FP detections during training. Finally, we fix the thresholds τ_{fp} for FP elimination, τ_{fn} for FN propagation, τ_{nb} for NB initialization, and τ_{dt} for DT termination with cross-validation. We found that $\tau_{fn} = 0.5$, $\tau_{nb} = 0.5$, and

$\tau_{dt} = 0.5$ works best for all classes; $\tau_{fp} = 0.7$ works best for all classes except for motorcycle and pedestrian, which are assigned $\tau_{fp} = 0.4$ and $\tau_{fp} = 0.6$ respectively.

C. Comparison with State-of-the-Art Tracking

Our nuScenes test results can be seen in Tables I and II. For the nuScenes test results, we compare our algorithm to trackers that use the CenterPoint [2] detections to ensure a fair comparison. [2] is our baseline, and we include recent, peer-reviewed works cited in Section II that tackle data association, track lifecycle management, FPs, and FNs with learning-based approaches in the LiDAR-only and multi-modal tracking domains. In Table I, we can see that ShaSTA balances correct tracking (AMOTA) with precise, high-quality tracking (AMOTP). Examining further metric breakdowns in Table II, it becomes clear that ShaSTA is effective in de-cluttering environments of FPs and compensating for missed detections to contribute to overall tracking improvement. The two most observed classes that constitute over 80% of the test set are cars and pedestrians, and we get highly competitive results in both of those categories, which tend to suffer from crowded scenes. ShaSTA performs well on all vehicles while achieving *the highest AMOTA on cars* across all LiDAR-only trackers for the nuScenes test set, according to the public leaderboard at the time of writing.

TABLE III: Ablation on nuScenes validation set for number of 3D bounding box points used to extract shape descriptors. Evaluation is in terms of overall AMOTA. The blue entry is our full method.

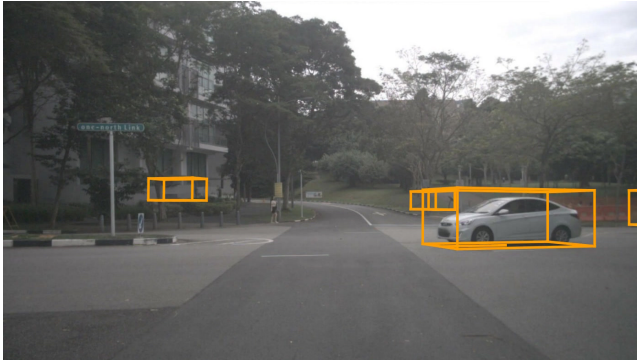
Box Center Used	Face Centers Used	AMOTA \uparrow
\checkmark	\times	69.5
\times	\checkmark	69.9
\checkmark	\checkmark	70.3

TABLE IV: Ablation on nuScenes validation set using learned affinity matrix for track formation. Evaluation is in terms of overall AMOTA. The blue entry is our full method.

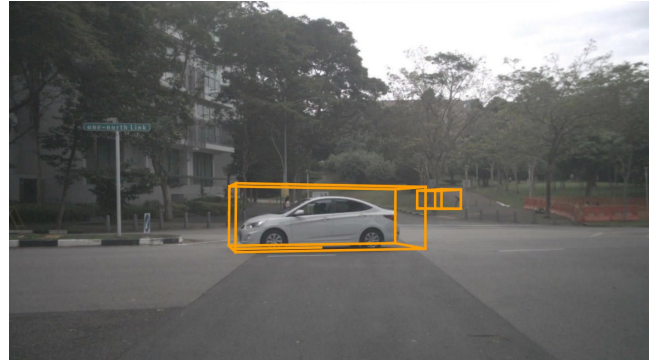
Affinity Augmentation Method	AMOTA \uparrow
False-Positive Elimination Only	70.1
False-Negative Propagation Only	68.0
Newborn Initialization Only	70.1
Dead Track Termination Only	67.9
All (ShaSTA)	70.3

D. Ablation Studies

We complete two ablative experiments on the nuScenes validation set to measure the impacts of (1) the number of 3D bounding box centers used to extract shape descriptors



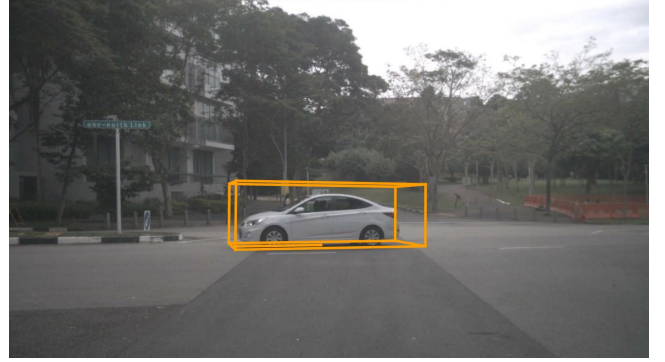
(a) CenterPoint: Scene 270, Frame 29



(b) CenterPoint: Scene 270, Frame 30



(c) ShaSTA: Scene 270, Frame 29



(d) ShaSTA: Scene 270, Frame 30

Fig. 3: Tracking visualization for cars projected onto front camera. We show two consecutive frames from Scene 270 of the validation set for CenterPoint [2] and ShaSTA. In frame 29, CenterPoint has 3 false-positive tracks as can be seen in (a), and one of the false-positives persists into frame 30 as illustrated in (b). However, (c), (d) show that ShaSTA perfectly tracks the car in both frames without any false-positives or false-negatives.

from the BEV map; and (2) including FP elimination, FN propagation, NB initialization, and DT termination. In Table III, we can see that as we add more bounding box centers for extracting shape descriptors, the accuracy of our model monotonically increases. This result supports our argument that leveraging raw sensor information to get spatio-temporal and shape information is integral to the success of our algorithm. Furthermore, in Table IV, we see that the most impactful augmentations are FP elimination and NB initialization. Eliminating FPs is expected to boost our accuracy since off-the-shelf detections suffer from such high rates of FP detections. NB initialization can be seen as a second reinforcement on eliminating FP detections because unmatched detections that do not have a probability of at least τ_{nb} for being NBs do not get initialized as tracks, and therefore, they get discarded. Finally, even though FNs and DT termination have not been as detrimental to tracking algorithms in the past, these augmentations alone give us competitive, state-of-the-art accuracies, showing that every augmentation in our technique contributes to effective tracking.

E. Qualitative Results

As indicated in Table I, there are significant increases in test accuracy from the CenterPoint [2] baseline, particularly for objects like cars and pedestrians that are more prone to being in crowded scenes and thus, have increased susceptibility to experiencing high rates of FP tracks.

Though the AMOTA metric does not strongly penalize FP tracks with low confidence scores, they are extremely

relevant to real-world deployment, as they can have detrimental effects on downstream decision-making tasks. Thus, in Figure 3, we emphasize the car results from validation scene 270. (a), (b) are two consecutive frames showing the CenterPoint [2] baseline which has false-positive tracks in both frames. On the other hand, (c), (d) demonstrate ShaSTA’s ability to declutter the scene and accurately track the car, while ignoring background information that should not be tracked. Typically, past works [26] use non-maximal suppression heuristics such as intersection over union (IoU) to remove false-positive tracks, but in more complex settings like scene 270, such heuristics would fail because none of the false-positive tracks overlap with other track predictions. As a result, ShaSTA proves to be especially effective at using shape and spatio-temporal information from LiDAR point clouds to localize and track actual objects of interest in the scene.

VI. CONCLUSION

We present ShaSTA, a 3D multi-object tracking technique that leverages shape and spatio-temporal information from LiDAR sensors to learn affinities for robust data association and track lifecycle management. Our approach effectively addresses false-positives and missing detections against cluttered scenes and occlusion, yielding state-of-the-art performance. Interesting future directions include the usage of our learned affinities in prediction and planning.

VII. ACKNOWLEDGMENT

Toyota Research Institute provided funds to support this work.

REFERENCES

- [1] M. Everingham, L. Van Gool, C. K. Williams, J. Winn, and A. Zisserman, "The pascal visual object classes (voc) challenge," *International journal of computer vision*, vol. 88, no. 2, pp. 303–338, 2010.
- [2] T. Yin, X. Zhou, and P. Krahenbuhl, "Center-based 3d object detection and tracking," in *Proceedings of the IEEE/CVF conference on computer vision and pattern recognition*, 2021, pp. 11 784–11 793.
- [3] Y. Zhou and O. Tuzel, "Voxelnet: End-to-end learning for point cloud based 3d object detection," in *Proceedings of the IEEE conference on computer vision and pattern recognition*, 2018, pp. 4490–4499.
- [4] J.-N. Zaech, A. Liniger, D. Dai, M. Danelljan, and L. Van Gool, "Learnable online graph representations for 3d multi-object tracking," *IEEE Robotics and Automation Letters*, vol. 7, no. 2, pp. 5103–5110, 2022.
- [5] F. Meyer, T. Kropfreiter, J. L. Williams, R. Lau, F. Hlawatsch, P. Braca, and M. Z. Win, "Message passing algorithms for scalable multitarget tracking," *Proceedings of the IEEE*, vol. 106, no. 2, pp. 221–259, 2018.
- [6] H.-k. Chiu, J. Li, R. Ambruş, and J. Bohg, "Probabilistic 3d multi-modal, multi-object tracking for autonomous driving," in *2021 IEEE International Conference on Robotics and Automation (ICRA)*. IEEE, 2021, pp. 14 227–14 233.
- [7] X. Wang, C. Fu, Z. Li, Y. Lai, and J. He, "Deepfusionmot: A 3d multi-object tracking framework based on camera-lidar fusion with deep association," *arXiv preprint arXiv:2202.12100*, 2022.
- [8] X. Weng, J. Wang, D. Held, and K. Kitani, "3D Multi-Object Tracking: A Baseline and New Evaluation Metrics," *IROS*, 2020.
- [9] M. Liang, B. Yang, W. Zeng, Y. Chen, R. Hu, S. Casas, and R. Urtasun, "Pnpnet: End-to-end perception and prediction with tracking in the loop," in *CVPR*, 2020.
- [10] R. Girshick, "Fast r-cnn," in *Proceedings of the IEEE international conference on computer vision*, 2015, pp. 1440–1448.
- [11] X. Zhou, D. Wang, and P. Krähenbühl, "Objects as points," in *arXiv preprint arXiv:1904.07850*, 2019.
- [12] C. R. Qi, H. Su, K. Mo, and L. J. Guibas, "Pointnet: Deep learning on point sets for 3d classification and segmentation," in *Proceedings of the IEEE conference on computer vision and pattern recognition*, 2017, pp. 652–660.
- [13] M. Engelcke, D. Rao, D. Z. Wang, C. H. Tong, and I. Posner, "Vote3deep: Fast object detection in 3d point clouds using efficient convolutional neural networks," in *2017 IEEE International Conference on Robotics and Automation (ICRA)*. IEEE, 2017, pp. 1355–1361.
- [14] B. Yang, W. Luo, and R. Urtasun, "Pixor: Real-time 3d object detection from point clouds," in *Proceedings of the IEEE conference on Computer Vision and Pattern Recognition*, 2018, pp. 7652–7660.
- [15] A. H. Lang, S. Vora, H. Caesar, L. Zhou, J. Yang, and O. Beijbom, "Pointpillars: Fast encoders for object detection from point clouds," in *Proceedings of the IEEE/CVF conference on computer vision and pattern recognition*, 2019, pp. 12 697–12 705.
- [16] H. Choi, M. Kang, Y. Kwon, and S.-e. Yoon, "An objectness score for accurate and fast detection during navigation," *arXiv preprint arXiv:1909.05626*, 2019.
- [17] C. R. Qi, O. Litany, K. He, and L. J. Guibas, "Deep hough voting for 3d object detection in point clouds," in *proceedings of the IEEE/CVF International Conference on Computer Vision*, 2019, pp. 9277–9286.
- [18] H.-k. Chiu, A. Prioletti, J. Li, and J. Bohg, "Probabilistic 3d multi-object tracking for autonomous driving," *arXiv preprint arXiv:2001.05673*, 2020.
- [19] X. Weng, Y. Wang, Y. Man, and K. Kitani, "Gnn3dmot: Graph neural network for 3d multi-object tracking with multi-feature learning," in *CVPR*, 2020.
- [20] A. Kim, A. Ošep, and L. Leal-Taixé, "Eagermot: 3d multi-object tracking via sensor fusion," in *2021 IEEE International Conference on Robotics and Automation (ICRA)*. IEEE, 2021, pp. 11 315–11 321.
- [21] X. Guo and Y. Yuan, "Joint class-affinity loss correction for robust medical image segmentation with noisy labels," *arXiv preprint arXiv:2206.07994*, 2022.
- [22] M. Hayat, S. Khan, W. Zamir, J. Shen, and L. Shao, "Max-margin class imbalanced learning with gaussian affinity," *arXiv preprint arXiv:1901.07711*, 2019.
- [23] S. Sun, N. Akhtar, H. Song, A. Mian, and M. Shah, "Deep affinity network for multiple object tracking," *IEEE transactions on pattern analysis and machine intelligence*, vol. 43, no. 1, pp. 104–119, 2019.
- [24] H. Caesar, V. Bankiti, A. H. Lang, S. Vora, V. E. Liong, Q. Xu, A. Krishnan, Y. Pan, G. Baldan, and O. Beijbom, "nusenes: A multimodal dataset for autonomous driving," in *Proceedings of the IEEE/CVF conference on computer vision and pattern recognition*, 2020, pp. 11 621–11 631.
- [25] X. Weng and K. Kitani, "A baseline for 3d multi-object tracking," *arXiv preprint arXiv:1907.03961*, vol. 1, no. 2, p. 6, 2019.
- [26] C. Stearns, D. Rempe, J. Li, R. Ambrus, S. Zakharov, V. Guizilini, Y. Yang, and L. J. Guibas, "Spot: Spatiotemporal modeling for 3d object tracking," *arXiv preprint arXiv:2207.05856*, 2022.